

STUDY OF DYNAMICS OF MICROSTRUCTURAL TRANSFORMATIONS IN CRYSTALLINE YTTRIA NANOPOWDER

R. P. Ermakov, P. P. Fedorov, V. V. Voronov

Prokhorov General Physics Institute, Russian Academy of Sciences, Moscow, Russia

x-ray_diffraction@mail.ru

PACS 61.05.C-

This paper is a continuation of a previously reported study of the microstructure transformations in crystalline yttria nanopowder prepared by soft chemistry via precipitation from aqueous acidic nitrates. We have observed the aforementioned transformations over extended periods of time at 900 °C and 1100 °C (isothermal annealing) with the use of X-ray diffraction analysis (full profile analysis of reflections, etc.).

Keywords: yttrium oxide, optical ceramics, X-ray diffraction phase analysis.

1. Introduction

This paper is a continuation of our previous studies [1] of transformations of the microstructure of crystalline yttria nanopowder at 600 °C and 800 °C during isothermal annealing. Such information is crucial for the preparation of yttria-based optical ceramics, which are more advantageous than single crystals of the same chemical composition [2–4]. Crystalline yttria nanopowders can easily be prepared by annealing yttrium hydroxynitrate, which is incidentally the most inexpensive yttria nanopowder precursor [5–10]. The latter has to satisfy very strict criteria of chemical purity and microstructure, and this is why studying the dynamics of structural transformations in yttria nanopowders under annealing is so important: it allows control over the properties of yttria nanopowder samples. Therefore, the topic of our study was X-ray diffraction analysis (including full profile analysis of reflections) and scanning electron microscopy investigation of domains of coherent scattering (DCS), their morphology and crystallite microdeformations under annealing at 900 °C and 1100 °C for 1–1440 minutes.

2. Experimental

Our experiments included the preparation of the starting yttrium hydroxynitrate by precipitation with aqueous ammonia from aqueous nitrate solutions, followed by conversion to crystalline yttria nanopowder via annealing. We used both 99.99% pure yttria and nitric acid as well as 99.5% pure ammonia as our starting materials. Component additions were controlled with a Hanna Instrument pH-meter (usually, pH values varied within 0.76–9.00 interval). Thermal treatment of the prepared samples was carried out in alumina crucibles in SNOL ovens under air. For detailed protocols of these syntheses please see our previous paper [1].

The phase composition and particle morphology of all synthesized samples were studied by X-ray diffraction analysis, transmission and scanning electron microscopy (TEM and SEM, respectively). We used Bruker D8 Discover A25 DaVinci Design ($\text{Cu}_{K\alpha}$ – radiation, standard Bragg-Brentano assembly) diffractometer for describing specimen microstructure dynamics and for estimating the content of X-ray amorphous phase in synthesized yttria nanopowder. Full profile analysis of the X-ray diffraction patterns was carried out using TOPAS [11, 12] and

FullProf [13] software (Pawley [14], LeBail [15] and modified Rietveld [16] techniques). TEM and SEM images were recorded using a Leo 912 AB Omega and NVision 40 microscopes.

3. Results and Discussion

3.1. Calculation of domains of coherent scattering (DCS) and microdeformations

Full-profile Rietveld analysis of X-ray pattern peak profiles was carried out using Voigt function approximation (a bundle of Cauchy and Gaussian functions). In turn, the Voigt function was approximated by pseudo-Voigt function (sum of Cauchy and Gaussian components) with inclusion Figner's divergence [17]. We assumed that the small size of DCS and microdeformations contributed to the broadening of both Voigt function components, but these contributions depended on the scattering angle in a different manner as per Scherrer and Stokes formulas:

$$\beta_{size} = \frac{\lambda}{D \cos(\theta)}, \quad (1)$$

$$\beta_{strain} = 2 \cdot e \cdot \tan(\theta), \quad (2)$$

where β_{size} , β_{strain} – integral broadening caused by size and deformation, respectively; λ – wavelength of monochromatic X-ray irradiation (nm); D – DCS size (nm); e – size of microdeformation. Taking into account equations (1) and (2) as well as the known empirical Cagliotti correlation between peak half-width and its location in the X-ray diffraction pattern, one can suggest the following formulas for Gaussian and Lorentzian half-widths and their dependency from the diffraction angle that were used in FullProf software:

$$H_G^2 = (U + (1 - \eta)^2 \cdot D_{st}^2(\alpha_D)) \cdot \tan^2(\theta) + V \cdot \tan(\theta) + W + \frac{Ig}{\cos^2(\theta)}, \quad (3)$$

$$H_L = (X + \eta \cdot D_{st}^2(\alpha_D)) \cdot \tan(\theta) + \frac{Y + F(sz)}{\cos(\theta)},$$

where H_G , H_L – contributions of the Gaussian and Lorentzian half-widths to the pseudo-Voigt functions, respectively; U , V , W – Cagliotti function parameters refined by cyclic least square technique (LST) for each individual X-ray diffraction pattern; η – weighted contribution of Lorentzian function; $D_{st}(\alpha_D)$, X – microdeformation parameters; Y , $F(sz)$, Ig – DCS parameters. Correct calculation of the DCS and microdeformation values also requires subtraction of the instrument contribution to the observed peak half-widths:

$$\begin{aligned} H_{G_sam}^2 &= H_{G_obs}^2 - H_{L_ins}^2, \\ H_{L_sam} &= H_{L_obs} - H_{L_ins}, \end{aligned} \quad (4)$$

where H_{G_sam} , H_{G_obs} , H_{G_ins} – Gaussian half-width of the sample itself, observed half-width and instrumental half-width, respectively; H_{L_sam} , H_{L_obs} , H_{L_ins} – Lorentzian half-width of the sample itself, observed half-width and instrumental half-width, respectively.

Instrument contributions to the peak half-widths were accounted for with the use of alumina specimen (NIST standard) prepared by a technique that excluded broadening lines in its X-ray diffraction pattern associated with DCS and microdeformations. We measured H_{G_ins} and H_{L_ins} for each peak in this alumina standard using profile fitting protocol from FullProf software assuming the following correlations between peak half-width and their reflection angles:

$$\begin{aligned} H_G^2 &= U \cdot \tan^2(\theta) + V \cdot \tan(\theta) + W, \\ H_L &= X \cdot \tan(\theta) + Y/\cos(\theta) + Z, \end{aligned} \quad (5)$$

where U, V, W, X, Y, Z – instrument function parameters, that were determined by LST for each measuring instrument.

We used a very similar approach earlier in analyzing X-ray diffraction patterns [1], but in the present paper we implemented more advanced software that provides better agreement with the experimental data and a better level of refinement for the calculated results.

3.2. Determination of mass content of amorphous phase

The content of the amorphous phase in a sample is the most important factor in powder technology, for it plays a crucial role in determining the mechanism of microstructure changes. There are many methods for evaluating amorphous phase content described in the literature based on the ratio of X-ray diffraction peak area(s) and area(s) of the background. This approach describes quite adequately the dynamics of changing aforementioned amorphous phase content in series of similar samples, but its accuracy is poor (ca. 20% error in determining the actual content of the amorphous phase). In order to remedy the latter drawback, we implemented our own technique of Rietveld-type quantitative phase analysis based on spiking the sample with an alumina standard, mixing it to a pseudo-homogeneous state and recording its X-ray diffraction pattern. If the following ratio:

$$\eta_{st} > \frac{m_{st}}{m_{st} + m_{samp}}, \quad (6)$$

where m_{samp} is a mass of the sample, m_{st} is a mass of spiking standard and η_{st} is a weight part of the standard experimentally determined by Rietveld-type method, is correct, then the sample has an amorphous phase. Content of the latter can be calculated as follows:

$$\eta_{amorphous} = 1 - (1 - \eta_{samp}) \frac{m_{samp} + m_{st}}{m_{samp}}, \quad (7)$$

with the relative error not exceeding 1.5%.

3.3. Analysis of basic yttrium hydroxynitrate microstructure

Usually, crystalline yttria nanopowder is prepared by annealing yttrium hydroxynitrate during its chemical synthesis. Prehistory of such yttria samples determines its microstructure and morphology features. For example, one can easily observe anisotropic peak broadening in the typical X-ray diffraction pattern of yttrium hydroxynitrate (Fig. 1).

Most probably, this is caused by anisotropy of the domains of coherent scattering (DCS) and microdeformations. Full-profile Pawley-type analysis of this pattern confirmed the anisotropic character of DCS in this sample (difference between experimental and calculated results is shown in Fig. 1, too). This conclusion was also proven by transmission electron microscopy (TEM) (Fig. 2): sample particles are shaped as ca. 10–13 nm thick platelets with ca. 300 nm diameters.

In other words, the platelet thickness is close to the smallest DCS values presented in Fig. 1. The fact that the other dimension size of the platelets (300 nm) is significantly different from the largest observed DCS value of 44 nm can be explained by differences in the platelets' spatial orientation and corresponding diffraction vector. It is very hard to tell anything about platelet orientation with respect to the crystal lattice axes, but the clear anisotropic broadening of diffraction peaks allows one to assume that all these platelets are somehow ordered, in a

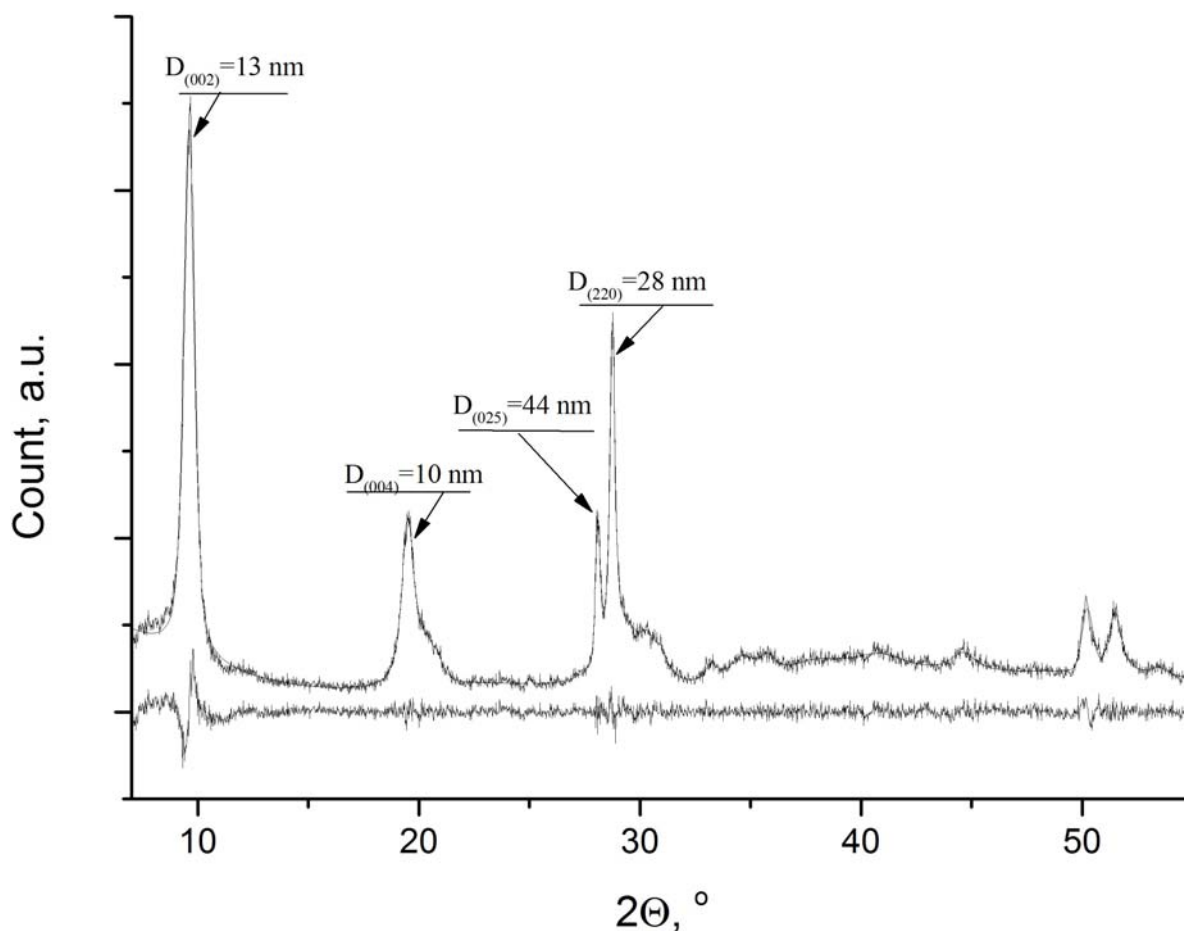


FIG. 1. X-Ray diffraction pattern of yttrium hydroxynitrate

similar spatial arrangement. Another suggestion one can make from the presented experimental data and agreement of the electron microscopy and X-ray diffraction studies results is that all these platelets form an area of coherent scattering (DCS), i.e., the unified crystalline space, not assembly of independent randomly oriented crystallites.

3.4. Dynamics of changes in the microstructure of yttria crystalline nanopowder during isothermal annealing at 900 °C

We studied the effects of isothermal annealing on the changes of yttria crystalline nanopowder microstructure by placing basic yttrium hydroxynitrate samples in a preheated 900 °C oven. Then, after a certain time, samples were retrieved from the heating chamber and studied by X-ray diffraction analysis. The results of this study are presented in Fig. 3.

These data unequivocally demonstrate that 900 °C isothermal annealing caused the formation of yttria in as short as 3 minutes. A further heating resulted only in an increase of the observed diffraction peaks' intensity and a decrease in their half-widths. Additional data, such as changes in a_0 lattice unit cell parameter, DCS, microdeformation values and content of amorphous phase over time are presented in Fig. 4.

They indicate that the content of amorphous phase in these yttria samples drops below 1% after annealing at 900 °C for 5 minutes. Lattice parameters decreased at the beginning of annealing and were stabilized after 300 min of heating. The most reasonable explanation for this fact is that the samples lost volatile components (e.g., water) at the beginning of annealing,

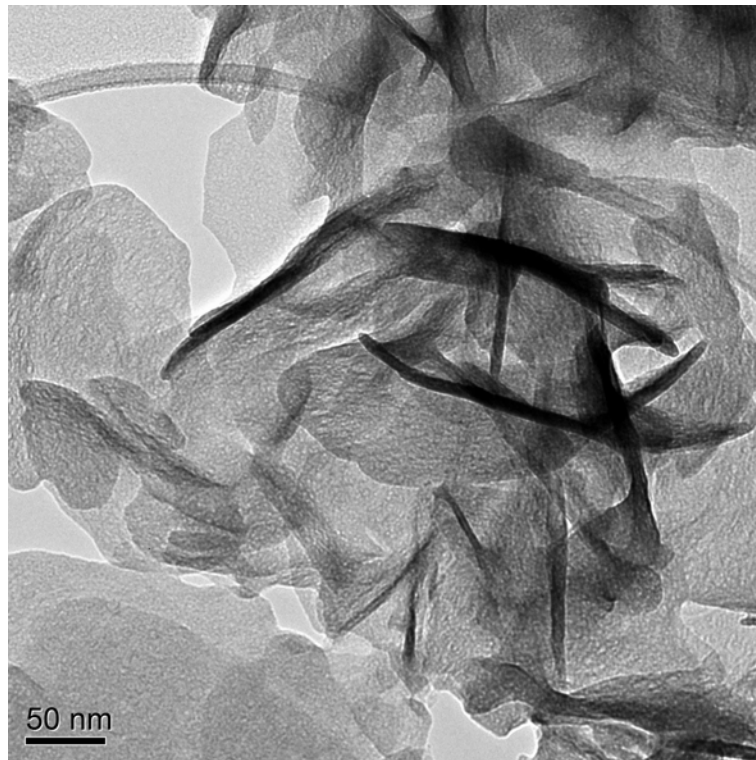


FIG. 2. Transmission electron microscopy (TEM) image of basic yttrium hydroxynitrate

and when there was nothing else to be excluded from the crystalline lattice, its parameter ceased to change. However, the simple presence of such volatiles guaranteed inhomogeneity of the chemical composition of yttria particles, and thus, produced microdeformations. In general, isothermal annealing of yttria leads to an increase of a size of the crystallites, perfecting the crystal order and making crystal composition even over the whole sample (Fig. 4). We have observed these phenomena in our experiments (Fig. 3 and 4). At the same time, it is worth noting that the growth of the DCS and decreasing microdeformation values over time is not steady for DCS (clear stepwise profile) whereas the microdeformations' decrease is relatively smooth.

Changes of the powder samples' microstructure can easily be analyzed with the use of Williamson-Hall charts [18]. If one assumes that the particles scattering X-rays are isotropic, containing evenly distributed microdeformations, then peaks in the diffraction patterns can be described by Lorentzian functions, permitting the use of the following equation:

$$\frac{\beta_{sam} \cos(\theta)}{\lambda} = \frac{1}{D} + \varepsilon \frac{2 \sin(\theta)}{\lambda}, \quad (8)$$

where β_{sam} – integral width of diffraction peak, which widening is caused by factors of size and microstructure. This equation can be easily transformed to a linear correlation in the following coordinates: $\frac{\beta_{sam} \cos(\theta)}{\lambda} = f\left(\frac{2 \sin(\theta)}{\lambda}\right)$, so the slope of the fitting line is proportional to microdeformations, whereas DCS is inversely proportional to the intercept.

Such charts prepared for 900 °C yttria isothermally annealed crystalline nanopowder (Fig. 5) showed very good linearity of experimental data (R^2 factor was close to 1.0 for all linear fits) and thus justified the use of an isotropic model for the DCS and microdeformation calculations. Lines in the Fig. 5 chart turn clockwise and shift down with an increase in the

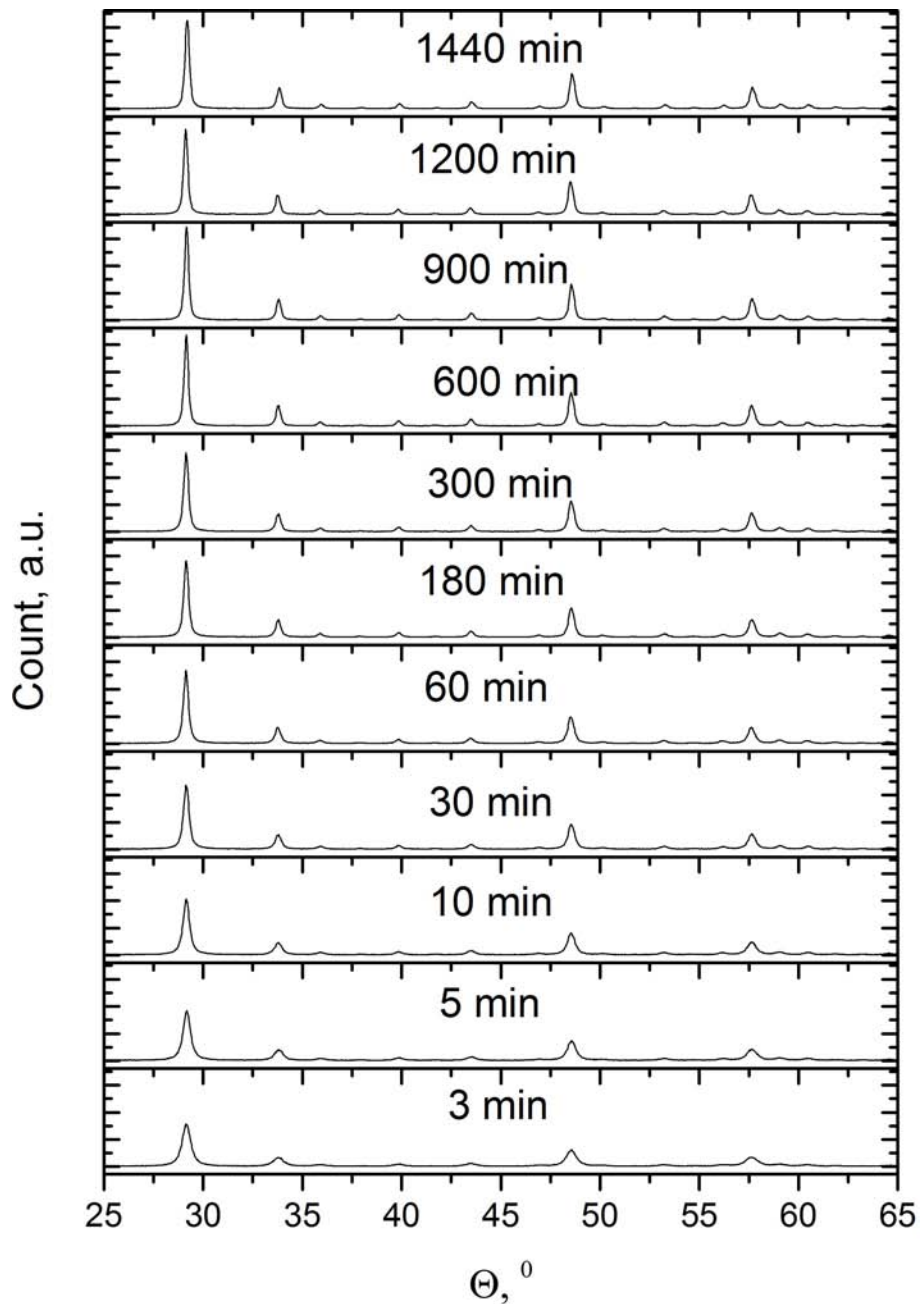


FIG. 3. X-Ray diffraction patterns of yttrium hydroxynitrate samples annealed at 900 °C for different times

annealing time, and these changes occur most notably at the beginning of annealing and after 300 min heating.

3.5. Dynamics of changes in the microstructure of yttria crystalline nanopowder during isothermal annealing at 1100 °C

Results for yttria annealing experiments at 1100 °C are very similar to those obtained at 900 °C (described above). We did not run special experiments to determine the content of the amorphous phase in the samples at the beginning of thermal treatment, for the amorphous phase disappeared at 1100 °C more quickly than the 5 min interval noted for 900 °C experiments, where amorphous components made up less than 1% of the samples after 5 min annealing.

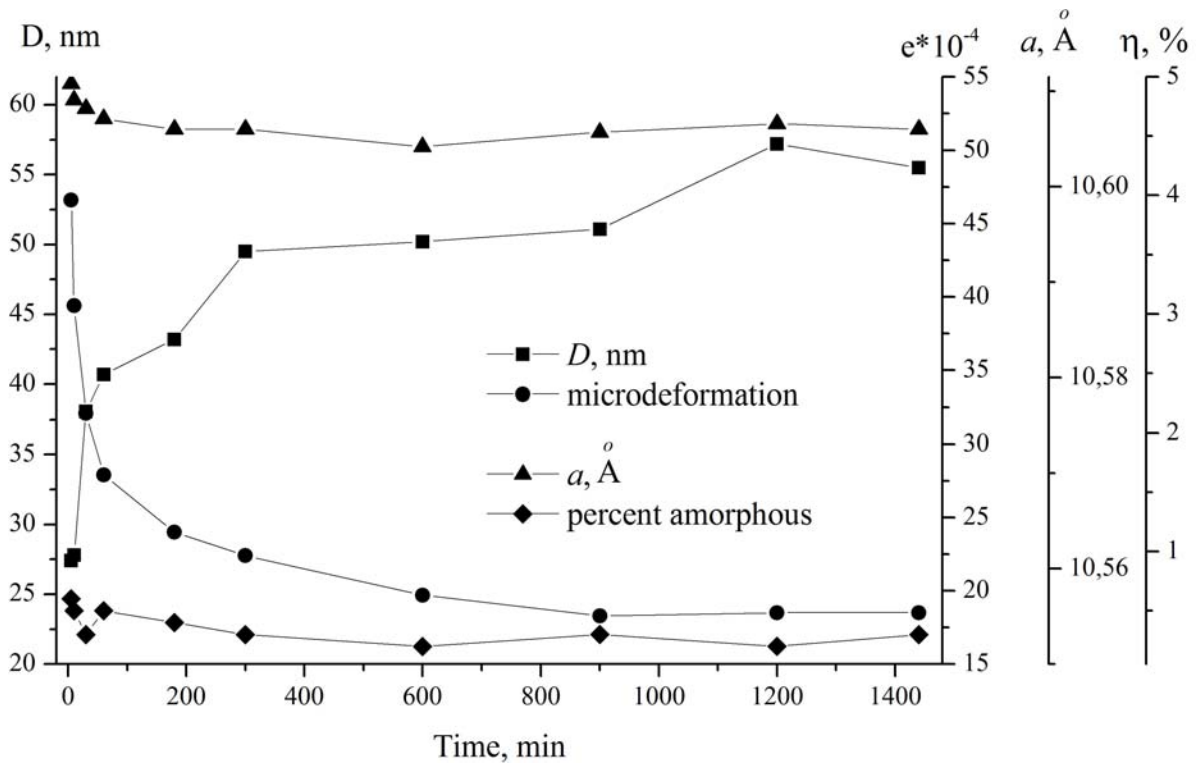


FIG. 4. Microstructure parameters of 900 °C annealed yttria crystalline nanopowder (D is the domains of coherent scattering (DCS), nm; a – cell parameter, Å)

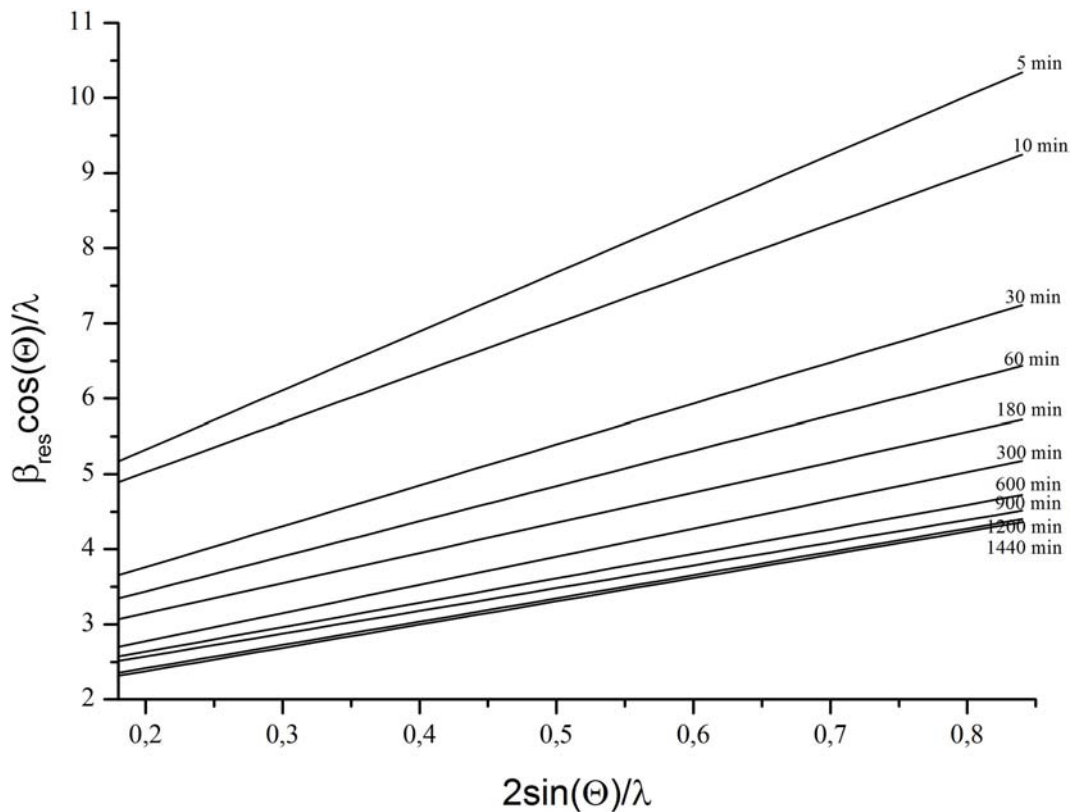


FIG. 5. Williamson-Hall charts for yttria crystalline nanopowder isothermally annealed at 900 °C

At 1100 °C, we observed the same dynamics of peak intensity growth and diminishing half-widths of diffraction lines (Fig. 6), and the most essential observation in these data was that diffraction peak broadening still remained after 420 min annealing.

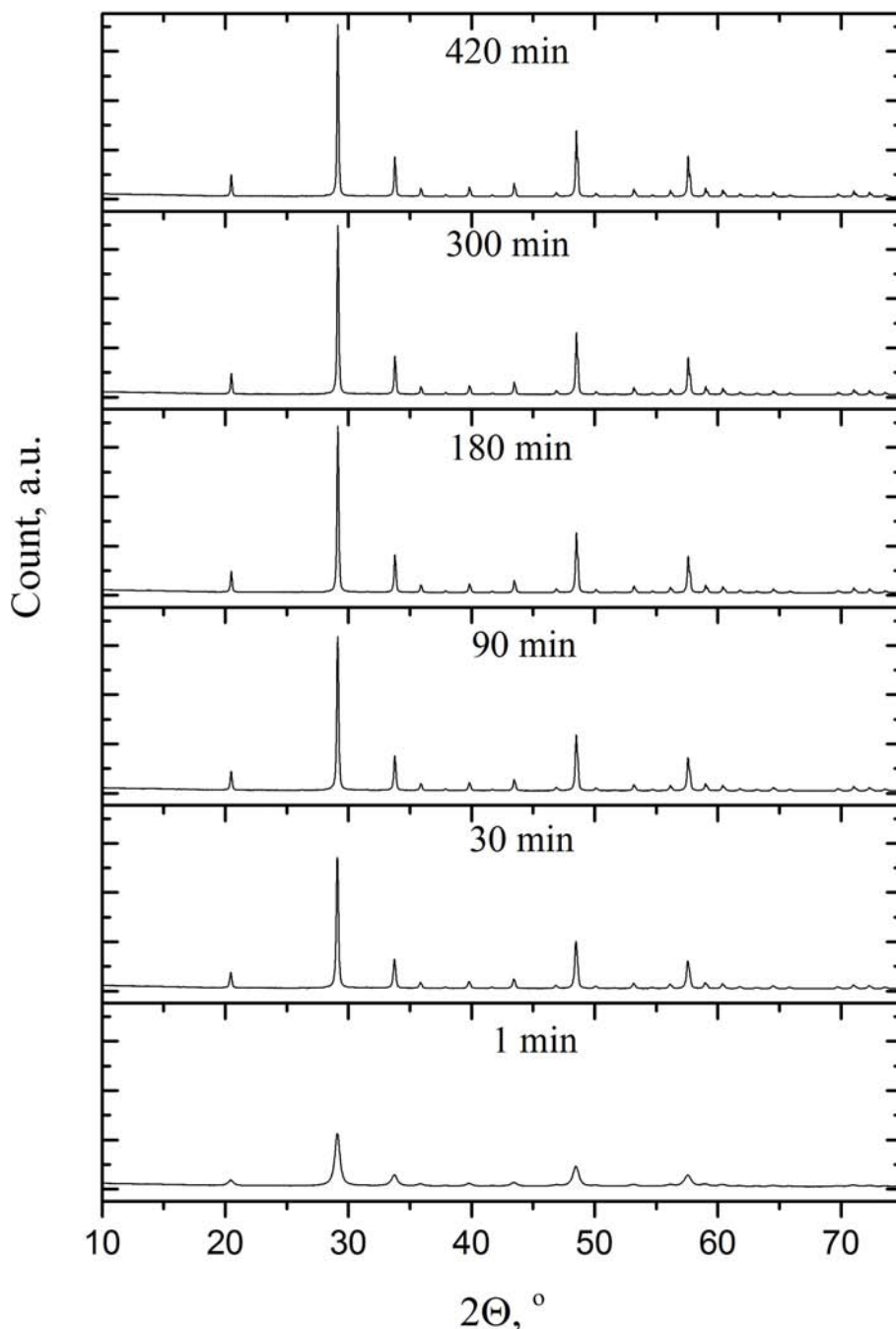


FIG. 6. Yttria nanopowder X-ray diffraction patterns after isothermal annealing at 1100 °C for different times

Scanning electron microscopy (SEM) study of 1100 °C annealed yttria nanoparticles has shown that at the earlier stages of thermal treatment, they possessed platelet shapes (Fig. 7a) – the same shape that existed for yttria precursor, basic yttrium hydroxynitrate. However, if hydroxynitrate demonstrated anisotropic DCS (e.g., see anisotropic diffraction peak broadening for basic yttrium hydroxynitrate in Fig. 1 and its particle images in Fig. 2), the formed yttria

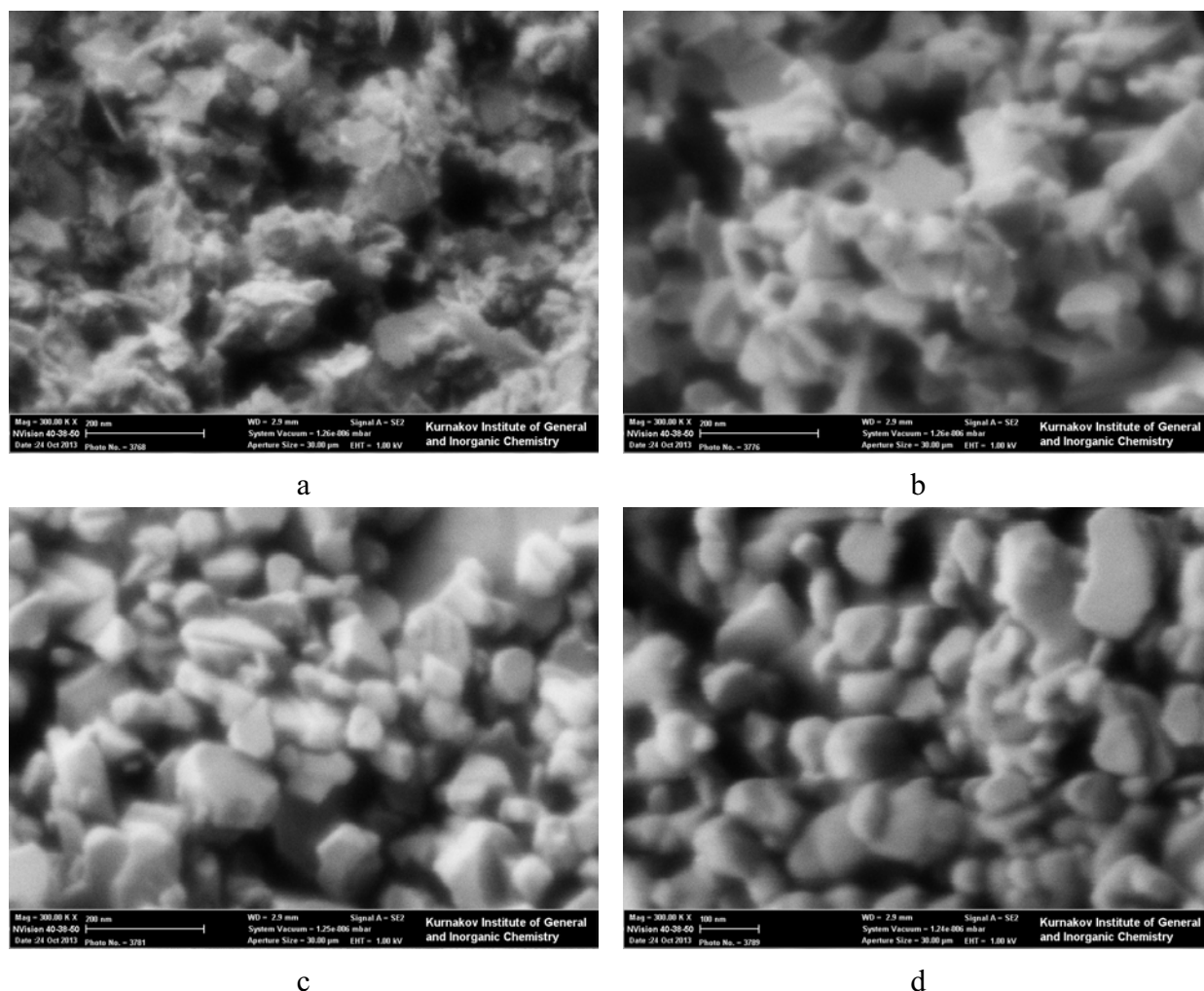


FIG. 7. Scanning electron microscopy (SEM) images of yttria nanoparticles annealed at 1100 °C for 1 min (a), 90 min (b), 300 min (c) and 420 min (d).

nanoparticles did not have such anisotropic character. It is quite probable that at the very early stage of the synthesis, in the course of basic nitrate thermolysis, yttria nanoparticles emerged from their precursor as polycrystalline aggregates made up of independent crystallites. Each platelet formed could have a texture that went undetected by X-ray diffraction method because these platelets were not mutually oriented. Yttria nanoparticles grow in size with increased annealing time, and one can clearly see this in Fig. 7b for the sample heated for 90 min: in addition to increasing the particle size, the deterioration of platelets as well as formation of sphere shaped nanoparticles and – somewhere – even crystal faces are quite visible. Further heating (Fig. 7c and 7d) led to the complete disappearance of the initial platelets and the formation of the larger properly shaped particles with clearly visible faces.

Changes in the microstructure and lattice parameters of 1100 °C annealed yttria nanoparticles are similar to the ones observed in 900 °C experiments (Fig. 8), including step-like changes for DCS values after the same 200 min annealing. Similarly, Williamson-Hall charts for 1100 °C experiments (Fig. 9) showed that the significant qualitative changes in particle microstructure occurred within first 30 min of thermal treatment. All linear fits in Fig. 9 had R^2 -factor close to 1.0 thus confirming applicability of isotropic approximation for nanoparticles and their microdeformations.

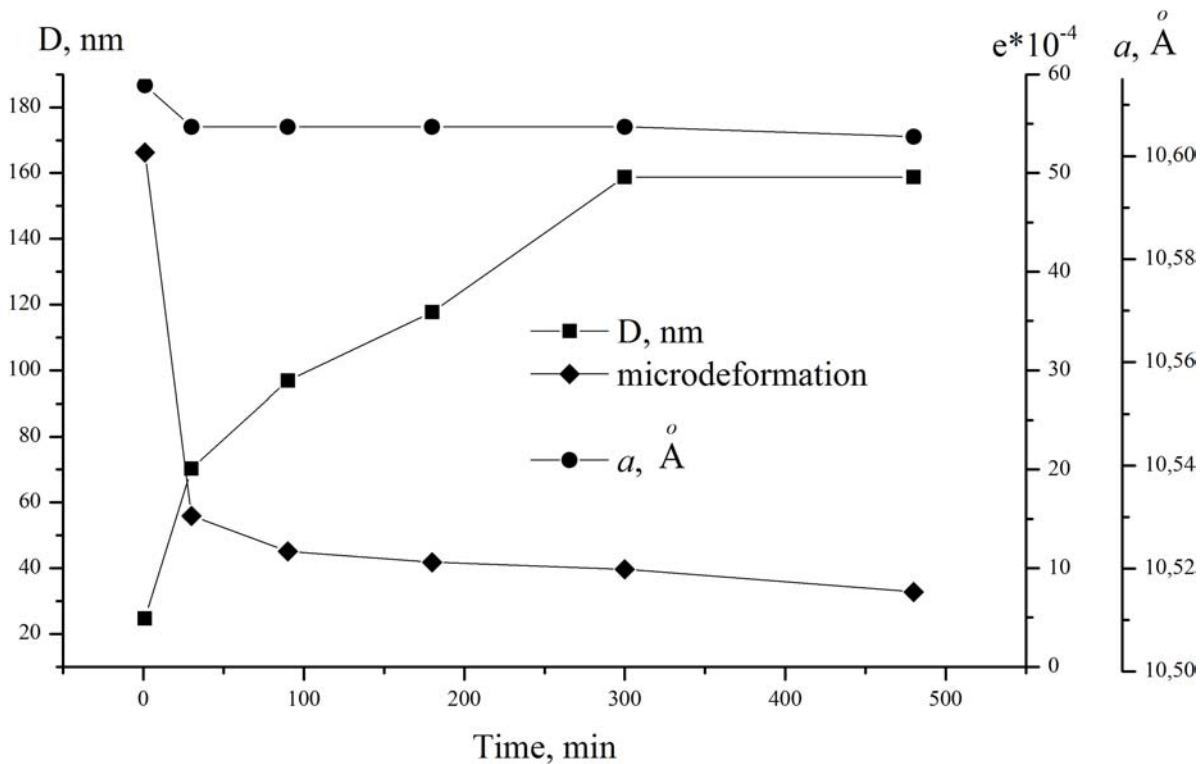


FIG. 8. Microstructure parameters of 1100 °C annealed yttria crystalline nanopowder (D is the domains of coherent scattering (DCS), nm; a – cell parameter, Å)

4. Conclusions

In conclusion, our study has confirmed that the yttria nanopowder precursor, yttrium basic hydroxynitrate, had a platelet morphology which was passed on to the newly-formed yttria nanoparticles during hydroxynitrate thermolysis. The fact that this platelet particle shape was retained at the earlier stages of yttria annealing is in complete agreement with the earlier results of Fedorov et al. [8].

Secondly, our experimental data have proven that the newly formed yttria nanocrystalline platelets were, in fact, polycrystalline aggregates of spherical crystallites incoherently scattering X-ray irradiation (yttria platelets could have had texture, too).

Thirdly, the above experimental data unequivocally indicate that the annealed yttria nanoparticles underwent fast DCS growth and a decline in microdeformations at the beginning of their thermal treatment. Further annealing caused only minor changes in the particle microstructure. This conclusion can be easily supported by the aforementioned Williamson-Hall charts (Figs. 4 and 8). We also suggest that for each annealing temperature, there will be the certain microstructure conditions that would remain unchanged, regardless of the duration of further isothermal annealing. The correlation between the sample's stationary state and its annealing temperature is presented in Fig. 10. However, in order to comment on this correlation and/or explain step-by-step character of DCS changes in the course of annealing, one needs to study the size distribution of the DCS in yttria nanosamples. The latter was outside of the scope of the present work, but will be addressed and discussed in our future publications.

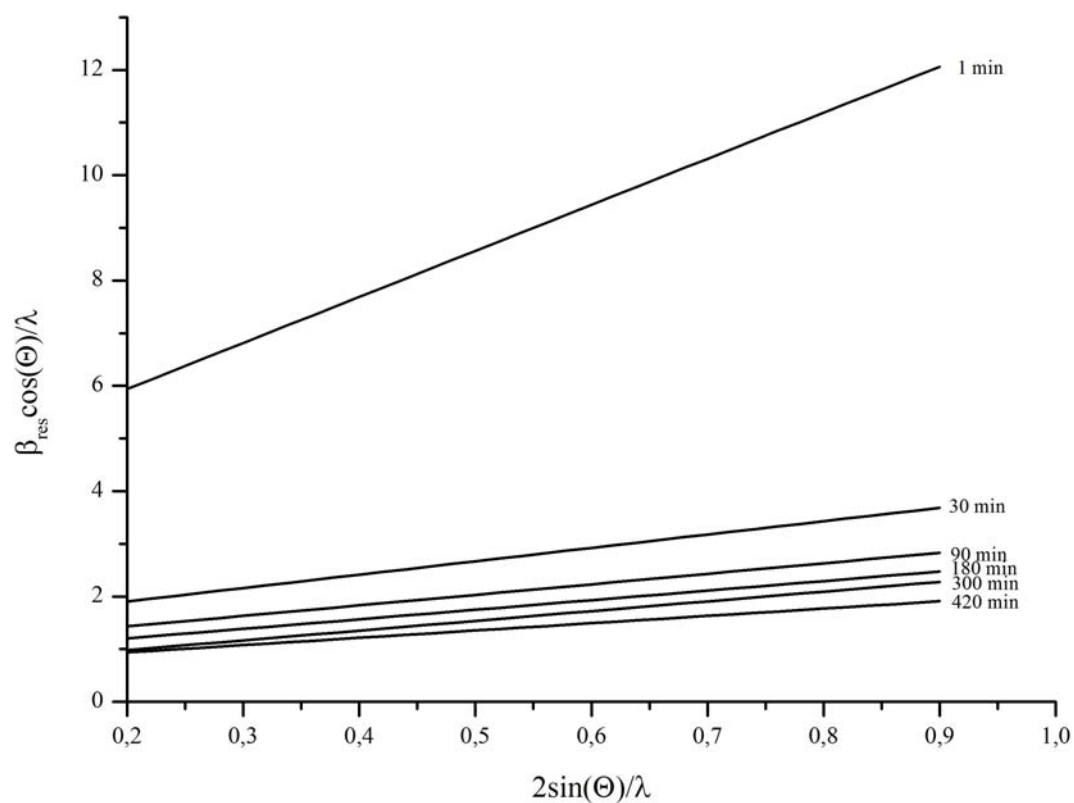


FIG. 9. Williamson-Hall charts for yttria crystalline nanopowder isothermally annealed at 1100 °C

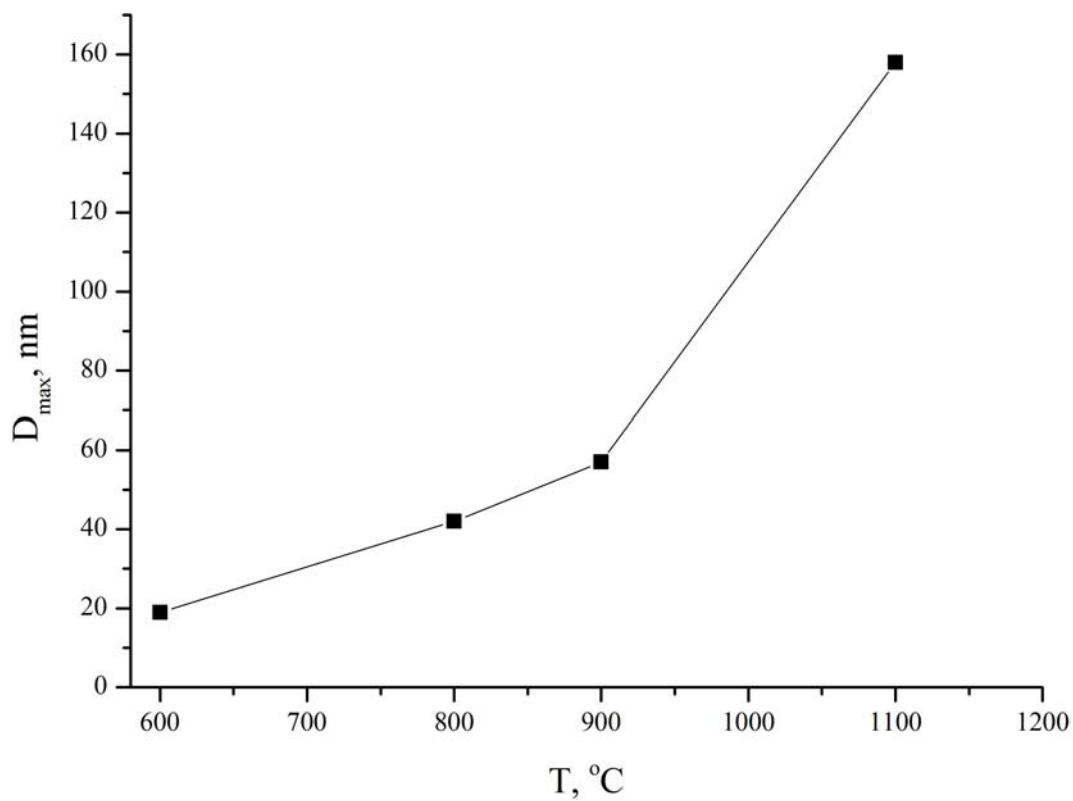


FIG. 10. Maximum DCS value of isothermally annealed yttria particles vs. annealing temperature

References

- [1] Ermakov R.P., Fedorov P.P., Voronov V.V. X-ray diffraction study of the phase and morphology changes in yttrium compound nanoparticles. *Nanosystems: physics, chemistry, mathematics*, **4** (2), P. 196–205 (2013).
- [2] Sanghera J., Shaw B., Kim W. et al. Ceramic laser materials. *Solid State Lasers XX: Technology and Devices*, Proc. SPIE 7912, 79121Q (2011).
- [3] Lupei V., Lupei A., Ikesue A. Single crystal and transparent ceramic Nd-doped oxide laser materials: a comparative spectroscopic investigation. *Journal of Alloys and Compounds*, **380**, P. 61–70 (2004).
- [4] Greskovich ., Chernoch J.P. Polycrystalline ceramic lasers. *J. Appl. Phys.*, **44**, P. 4599–4606 (1973).
- [5] Ikegami T., Mori T., Li J., Moriyoshi Y. Fabrication of transparent yttria ceramics by the low-temperature synthesis of yttrium hydroxide. *J. Amer. Ceram. Soc.*, **85**, P. 1725–1729 (2002).
- [6] Mouzon J. Synthesis of Yb: Y₂O₃ Nanoparticles and Fabrication of Transparent polycrystalline yttria ceramics. Thesis. Lulea University of Technology. Sweden (2005).
- [7] Baranchikov A. E., Ivanov V. K., Dmitriev A. V., et al. Chemical transformations of basic yttrium nitrates during ultrasonic-hydrothermal treatment. *Russian J. Inorg. Chem.*, **51** (11), P. 1689–1695 (2006).
- [8] Fedorov P.P., Voronov V.V., et al. Evolution of Yttria nanoparticle ensembles. *Nanotechnologies in Russia*, **5** (9–10), P. 624–634 (2010).
- [9] Ivanov V. K., Baranchikov A. E., Vanetsev A. S. et al. Effect of hydrothermal and ultrasonic/hydrothermal treatment on the phase composition and micromorphology of yttrium hydroxocarbonate. *Russian J. Inorg. Chem.*, **52** (9), P. 1321–1327 (2007).
- [10] Fedorov P. P., Tkachenko E. A., et al. Yttrium Oxide Nanopowders from Carbonate Precursors. *Russian J. Inorg. Chem.*, **55** (6), P. 883–889 (2010).
- [11] Cheary R.W., Coelho A.A. A fundamental parameters approach to X-ray line-profile fitting. *J. Appl. Cryst.*, **25**, P. 109–121 (1992).
- [12] Cheary R.W., Coelho A.A., Cline J.P. Fundamental Parameters Line Profile Fitting in Laboratory Diffractometers. *J. Res. Natl. Inst. Standt. Technol.*, **109**, P. 1–25 (2004).
- [13] Rodriguez-Carvajal J., Roisnel T. Line broadening analysis using FullProf*: Determination of microstructural properties. *European powder diffraction Epcdic*, **443** (4), P. 123–126 (2004).
- [14] Pawley G.S. Unit-cell refinement from powder diffraction scans. *J. Appl. Cryst.*, **14**, P. 357–361 (1981).
- [15] LeBail A., Duroy H., Fourquet J.L. Abinitio structure determination of LiSbWO₄ by X-ray powder diffraction. *Mat. Res. Bull.*, **23**, P. 447–452 (1998).
- [16] Rietveld H.M. A profile refinement method for nuclear and magnetic structures. *J. Appl. Cryst.*, **2**, P. 65–71 (1969).
- [17] Finger L.W. PROFVAL: functions to calculate powder-pattern peak profiles with axial divergence asymmetry, *J. Appl. Cryst.*, **31**, P. 111 (1998).
- [18] Williamson G.K., Hall W.H. X-ray line broadening from filed aluminium and wolfram. *Acta Metallurgica*, **1**, P. 22–31 (1953).